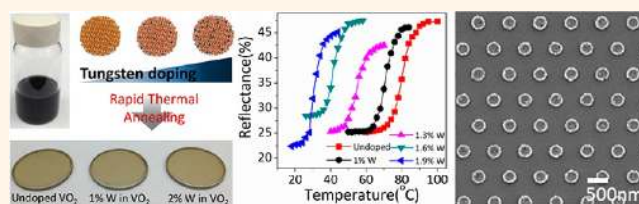


Solution-Processed Phase-Change VO₂ Metamaterials from Colloidal Vanadium Oxide (VO_x) Nanocrystals

Taejong Paik,^{†,¶} Sung-Hoon Hong,^{‡,¶,#} E. Ashley Gaulding,[§] Humeyra Caglayan,[‡] Thomas R. Gordon,[†] Nader Engheta,^{‡,§,⊥,||} Cherie R. Kagan,^{†,‡,§,*} and Christopher B. Murray^{†,§,*}

[†]Department of Chemistry, [‡]Department of Electrical and Systems Engineering, [§]Department of Materials Science and Engineering, [⊥]Department of Physics and Astronomy, and ^{||}Department of Bioengineering, University of Pennsylvania, Philadelphia, Pennsylvania 19104, United States. [¶]These authors contributed equally to this work. [#]Present address: Components & Materials Research Laboratory, Electronics and Telecommunication Research Institute (ETRI), Daejeon 305-350, Republic of Korea.

ABSTRACT We demonstrate thermally switchable VO₂ metamaterials fabricated using solution-processable colloidal nanocrystals (NCs). Vanadium oxide (VO_x) NCs are synthesized through a nonhydrolytic reaction and deposited from stable colloidal dispersions to form NC thin films. Rapid thermal annealing transforms the VO_x NC thin films into monoclinic, nanocrystalline VO₂ thin films that



show a sharp, reversible metal–insulator phase transition. Introduction of precise concentrations of tungsten dopings into the colloidal VO_x NCs enables the still sharp phase transition of the VO₂ thin films to be tuned to lower temperatures as the doping level increases. We fabricate “smart”, differentially doped, multilayered VO₂ films to program the phase and therefore the metal–insulator behavior of constituent vertically structured layers with temperature. With increasing temperature, we tailored the optical response of multilayered films in the near-IR and IR regions from that of a strong light absorber, in a metal–insulator structure, to that of a Drude-like reflector, characteristic of a pure metallic structure. We demonstrate that nanocrystal-based nanoimprinting can be employed to pattern multilayered subwavelength nanostructures, such as three-dimensional VO₂ nanopillar arrays, that exhibit plasmonic dipolar responses tunable with a temperature change.

KEYWORDS: vanadium dioxide · tungsten doping · phase transition · nanoimprinting · plasmonic

Metamaterials are artificial materials rationally designed from subwavelength nanostructures to engineer novel optical properties and to control the interaction of electromagnetic radiation with matter.^{1–3} They have been explored for various applications, including negative index metamaterials,^{4–6} perfect lenses,^{7,8} cloaking,^{9,10} and sensing devices.^{11,12} In most cases, the optical responses of metamaterials are fixed by the structure and electronic properties of the constituent engineered building blocks. Increasingly, there is a desire to realize dynamically tunable or switchable structures.^{13–16} Phase-change materials have been extensively studied to provide tuning/switching capabilities in optical systems and metamaterials.^{17–20} The physical properties of phase-change materials are switched in real-time during a structural phase transition (*e.g.*, crystalline to amorphous²¹ or between two distinct

crystalline forms²²), which allows optical responses such as a resonance wavelength to be dynamically modulated by external stimuli.

Vanadium dioxide (VO₂) is a promising phase-change material to use as a building block in reconfigurable metamaterials. In bulk, VO₂ exhibits at low temperature (68 °C) a reversible first-order metal–insulator phase transition,²³ from the semiconducting monoclinic (M1, space group *P2₁/c*) to metallic tetragonal (R, space group *P4₂/mmm*) structure, giving rise to a sharp change in optical and electrical properties. This phase transition can be triggered by many different types of stimuli such as heat,²⁴ mechanical strain,^{25,26} and electric field^{27–29} and has been applied in many emerging technologies, such as smart windows,^{30,31} optical switches,^{32,33} memory devices,^{34,35} and Mott transistors.^{36,37} Through micro- and nanofabrication methods, various tunable metamaterials have been

* Address correspondence to cbmurray@sas.upenn.edu, kagan@seas.upenn.edu.

Received for review October 18, 2013 and accepted December 30, 2013.

Published online December 30, 2013
10.1021/nn4054446

© 2013 American Chemical Society

demonstrated by the integration of phase-change VO_2 ,^{38–40} such as plasmonic modulators composed of gold or silver nanoantennae on VO_2 substrates,^{41,42} and as index modulators in plasmonic waveguides.⁴³ Phase-change VO_2 films are fabricated by a variety of techniques including the sol–gel method,^{44,45} ion implantation,⁴⁶ magnetron sputtering,⁴⁷ chemical vapor deposition (CVD),⁴⁸ and pulsed laser deposition (PLD).⁴⁹ The properties of VO_2 are further tailored by chemical doping of the VO_2 matrix to modify the phase transition temperature (T_c),⁵⁰ offering an additional degree of freedom to engineer the optical responses of metamaterials. However, to expand the application of VO_2 in nanostructured devices, it is essential to develop simple, scalable, and reproducible techniques to incorporate phase-change VO_2 into complex architectures and thus to allow precise engineering of the optical properties of large area surfaces.

Here, we present a solution-based process to fabricate phase-change VO_2 thin films and nanostructures using colloidal vanadium oxide (VO_x) NCs. Solution-based processes utilizing NC precursors offer the potential for low-cost, robust fabrication of highly reproducible films by scalable deposition techniques such as spin-coating and dip-coating,^{51,52} and patterning techniques such as inkjet printing⁵³ or direct writing.⁵⁴ VO_x NCs are synthesized using solution-based colloidal synthesis. Stable suspensions of colloidal VO_x NCs are readily deposited on substrates and transformed into phase-change monoclinic VO_2 (M1, space group $P2_1/c$) through thermal annealing, resulting in high-quality optical films over large areas. In addition, we investigate the effect of tungsten (W) doping on the phase transition behavior through systematic control of the dopant concentration during NC synthesis. Solution-based fabrication and controlled doping enables the integration of VO_2 building blocks into thermally responsive (“smart”) optical materials and patterning into geometrically tailored, subwavelength nanostructured reconfigurable materials by nanoimprinting techniques.

RESULTS AND DISCUSSION

Vanadium oxide (VO_x) NCs are synthesized through the high-temperature thermal decomposition of vanadium oxychloride (VOCl_3) in the presence of the solvent mixture 1-octadecanol and oleylamine. No reaction occurs in the absence of 1-octadecanol, which reveals that vanadium oxygen bonds form through the nonhydrolytic reaction between the metal halide and a primary alcohol.⁵⁵ Figure 1a displays transmission electron microscopy (TEM) images of synthesized VO_x NCs. VO_x NCs exhibit excellent colloidal stability in nonpolar solvents due to the oleylamine surfactants capping the NC surface (Figure 1b). Colloidal VO_x NC dispersions were deposited by spin-coating for structural, optical, and electrical characterization. Since many different

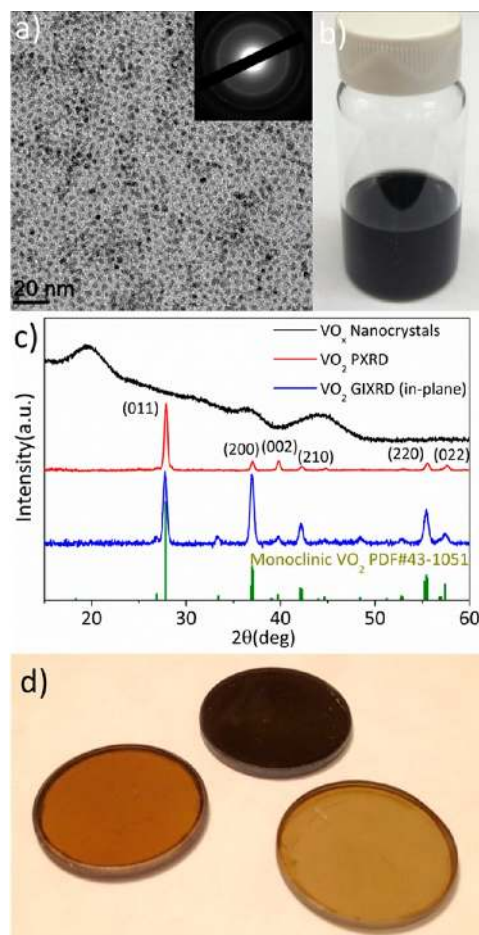


Figure 1. (a) TEM image of vanadium oxide (VO_x) NCs. The inset shows selected area electron diffraction. (b) Photograph of VO_x NCs dispersed in hexane. (c) PXRD and in-plane XRD patterns before and after thermal annealing of VO_x NCs on SiO_2/Si wafer. (d) Monoclinic VO_2 thin films obtained by rapid thermal annealing of VO_x NCs spin-coated on fused quartz substrates with varying thickness.

phases of vanadium oxide exist as stable polymorphs at room temperature and with various oxidation states, it is nontrivial to identify the crystal structure of the synthesized VO_x NCs.^{56,57} However, the diffraction peaks observed by powder X-ray diffraction (PXRD) measurements indicate that the VO_x NCs are crystalline (Figure 1c). This is also corroborated by selected area electron diffraction (SAED) (Figure 1a, inset) and high-resolution transmission electron microscopy (Supporting Information Figure S1). The average NC size calculated from small-angle X-ray scattering measurements is 4.3 ± 1.0 nm (Supporting Information Figure S2).

Since the crystal structure of colloidal VO_x NCs differs from the switchable, monoclinic phase VO_2 , thermal annealing is used to transform the films. Phase-change monoclinic VO_2 (M1, space group $P2_1/c$) thin films are obtained from spin-coated colloidal VO_x NC films after rapid thermal annealing (RTA), typically at 500 °C for 5 min, 450 °C for 30 min, and 400 °C for an hour under a reduced oxygen environment of 1 mmHg of air

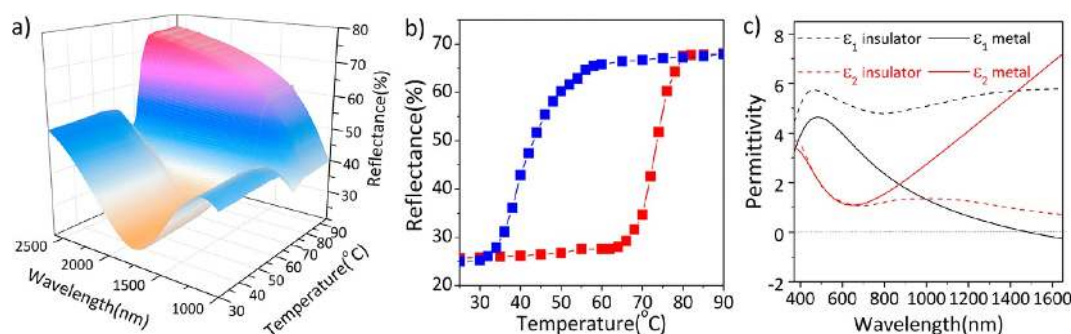


Figure 2. (a) Temperature-dependent optical reflectance of a VO₂ thin film and (b) its hysteresis recorded at 1550 nm. Reflectance spectra are measured in a specular reflection geometry at 45° to the normal direction. (c) Dielectric constant ($\epsilon = \epsilon_1 + i\epsilon_2$) of insulating and metallic VO₂ thin films, extracted from spectroscopic ellipsometry measurements.

(Figure 1d). The presence of some oxygen is critical, not only to remove organic surfactants from the NC surface but also to induce the structural transformation from VO_x into monoclinic VO₂. This suggests that the stoichiometry of as-synthesized NCs is a slightly oxygen-deficient VO₂. The approach utilizing colloidal NCs provides a potential for large-area, low-cost, and scalable processes on various substrates such as fused quartz, Si wafers, mica, and c-cut sapphire. In addition, the thickness of VO₂ thin films is readily and reproducibly controlled by changing the deposition conditions such as spin-coating rate or the concentration of NCs in the solution used for the deposition.

PXRD patterns, in Figure 1c, show that monoclinic VO₂ is obtained after RTA treatment of VO_x thin films. All diffraction peaks match the monoclinic VO₂ structure (M1, space group *P2₁/c*) without any noticeable minority phases or indications of an amorphous background. Preferred orientation of the VO₂ thin film is observed when deposited on SiO₂/Si wafers. Polycrystalline VO₂ thin films are characterized with conventional PXRD and in-plane X-ray diffraction (in-plane XRD) in order to probe the crystallographic orientation of VO₂ grains. Crystal planes aligned perpendicular to the substrate are monitored by PXRD, while in-plane orientation is determined by in-plane XRD. From the two complementary measurements, preferred orientation is characterized by comparing the intensities of diffraction peaks from different crystal planes. The diffraction intensities of the (011) plane relative to the (200) plane in PXRD measurements is much higher than in the in-plane XRD measurement, which suggests that VO_x NCs are transformed into monoclinic VO₂ with a preferred orientation of the VO₂ (011) zone axis aligned perpendicular to the substrate surface during thermal annealing. This preferential orientation is also observed in films deposited on fused quartz and c-cut sapphire (Supporting Information Figures S3 and S4). The effect of the substrate on the epitaxial growth of VO₂ thin films has previously been reported with contrasting findings. For example, polycrystalline VO₂ thin films deposited on c-Al₂O₃ by pulsed laser deposition^{58,59} and rf sputtering⁶⁰ show growth of the VO₂

film normal to the substrate in the (002)/(020) direction. However, polycrystalline VO₂ thin films on fused quartz, Si wafers, and c-sapphire, which are prepared by rapid thermal annealing of colloidal NCs, show similar diffraction patterns, suggesting that the crystal orientation may not be strongly affected by the substrate.

The optical properties of the VO₂ thin films are investigated by variable temperature-specular reflectance using a Fourier transform infrared (FTIR) spectrometer. Reflectance spectra are collected in the specular reflection geometry with a 45° incident angle using a gold mirror as the reflectance standard. A thin graphite disk is placed between the sample and the aluminum heating stage in order to prevent back reflection while maintaining efficient heat transport from the heater to the sample. The temperature of the VO₂ films is monitored through a thermocouple attached directly to the VO₂ film surface. Figure 2a shows optical reflectance spectra of a VO₂ thin film deposited on a fused quartz substrate as the sample temperature is increased. At room temperature, a fringe pattern is observed with the peak and valley located at 1128 and 1732 nm, respectively, which are caused by interference between light reflected from the top and bottom of thin films in the insulating phase.⁵⁹ At temperatures higher than *T_c*, the oscillatory interference pattern disappears as the reflectance in the IR region increases sharply due to strong reflectance from the metallic VO₂ phase. Similar trends are observed in transmittance measurements (Supporting Information Figure S5).

When the optical properties of the VO₂ films are measured while the sample is cooling, a significantly lower transition temperature is observed upon switching from the metallic to the insulating phase, indicating a wide hysteresis in the phase change. The width of the hysteresis during the cooling and heating cycle is about 25–30 K in undoped VO₂ films (Figure 2b and Supporting Information Figures S6 and S7). The hysteresis width is known to decrease with increasing grain size as defects and strain at grain boundaries contribute to the energy barrier for the phase transition.^{61–63}

Atomic force microscopy images reveal that the average grain size after 5 min of rapid thermal annealing is approximately 37 nm with a standard deviation of 8.7 nm (Supporting Information Figure S8). Although the growth in grain size is observed with longer annealing, RTA preserves the small grain size in the films annealed at even higher temperatures, for example, 550 °C for 5 min. The nanosized grains that are still preserved in the thin films may cause the large hysteresis between heating and cooling cycles. The large hysteresis could be useful in the design of an optical memory, allowing for nonvolatile storage of optical information during the phase transition.³⁵

The optical constants of both the insulating and metallic phases of VO₂ are extracted using spectroscopic ellipsometry (Figure 2c). The complex permittivity of the samples is extracted by fitting the optical response of thin films with a Lorentz–Lorentz model, in the case of the insulating phase, and a Drude–Lorentz model, in the case of the metallic phase. Below T_c , the real part of permittivity is positive over the entire spectral range measured from 400 to 1650 nm, indicating the dielectric response of the insulating, monoclinic VO₂ phase. At temperatures higher than T_c , the real part of the permittivity becomes negative in the near-IR region beyond the crossover energy of 0.86 eV, confirming optically the metallic response of tetragonal VO₂(R). The negative permittivity of our metallic phase VO₂ allows it to be incorporated as a switchable plasmonic building block in the near-IR and IR region.

Controlled doping into the VO₂ lattice is important not only to tailor T_c but also to modify the optical and electrical properties of VO₂.^{64,65} NC doping is a technique commonly used to tune electrical,^{66,67} optical,^{68–70} and magnetic properties.^{71,72} Colloidal synthetic methods allow for the homogeneous incorporation of dopants or defects into the lattices of a single NC. Since we use VO_x NCs as precursors for the fabrication of VO₂ thin films, it is possible to systematically control the type and concentration of transition metal dopants by simply changing the concentration of metal precursors during NC synthesis. Tungsten-doped VO_x NCs are synthesized by the addition of tungsten hexachloride (WCl₆) as the W source for the reaction; otherwise, the conditions are identical to those used for undoped VO_x. Energy-dispersive X-ray spectroscopy (EDS) reveals that the ratio of W and V precursors is maintained after the formation of the NCs, and TEM images show that there is no discernible change in NC size and shape due to the addition of W into the matrix (Supporting Information Figure S9). W-doped VO₂ thin films after RTA treatment are of the same high surface uniformity with similar grain sizes as the undoped films (Supporting Information Figure S10). The surface roughness as characterized by atomic force microscopy is about 2.7 nm for 1.9% W-doped VO₂, which is similar to the 1.7 nm found for

undoped VO₂ (Supporting Information Figure S8). Since W dopants are already distributed in the NC precursors with controlled stoichiometry, the transformed polycrystalline thin films may maintain a statistically uniform distribution of W dopants. In addition, high heating rates in RTA could help minimize thermal diffusion of W dopants, which can prevent phase segregation or local inhomogeneity of the W distribution in the VO₂ matrix.

Figure 3 displays the variable-temperature reflectance of W-doped VO₂ thin films deposited on fused quartz substrates. A decrease in T_c is observed with an increase in W doping concentration in VO₂. It has been reported that increasing the doping concentration causes broadening of the temperature range in which the phase transition occurs and reduces the degree of property change across the transition.⁷³ However, we observe that a steep change in reflectance across the phase transition is maintained in W-doped VO₂ thin films formed from the colloidal NCs, similar to that in undoped VO₂. Figure 3b presents the first derivative of the optical reflectance (dR/dT) of W-doped thin films as a function of doping concentration. The full width at half-maximum (fwhm) of dR/dT is similar between the 0 and 1.9% (atomic %) doping concentrations that we explored. The same trend is also observed in the electrical measurements. The temperature-dependent resistivity of W-doped VO₂ thin films is investigated using the van der Pauw method. Figure 3c displays the electrical resistivity of W-doped VO₂ over a range of temperatures from 5 to 100 °C. It is observed that an increase in doping concentration leads to a decrease in T_c while maintaining the fwhm of $d\rho/dT$, matching the trend observed by optical reflectance.

A series of colloidal NC solutions, in which the stoichiometry of V and W are systematically varied, can be readily processed as on-demand NC inks by solution-based processes. This allows for the simple, robust, and reproducible integration of doped VO₂ into complex architectures for metamaterials. We employ this technique to build multilayered VO₂ nanostructures by sequential deposition of VO₂ with different doping concentrations. Layered films composed of metal and dielectric layers are technologically important as they allow the engineering of transmittance, reflectance, and absorption for applications in antireflective coatings,⁷⁴ 2-D waveguides,⁷⁵ and perfect light absorbers.⁷⁶ A multilayered VO₂ nanostructure composed of 1.9% W, 1.3% W, and undoped layers is fabricated by sequential spin-coating of colloidal NCs at 1500 rpm for 30 s followed by RTA at 500 °C for 5 min after the deposition of each layer. The T_c of each layer is 30, 52, and 80 °C, respectively. Since the metallic and dielectric properties of W-doped VO₂ may be dynamically switched at T_c , this integrated layered structure incorporating different doping concentrations allows for layers that can be independently switched at different phase transition temperatures.

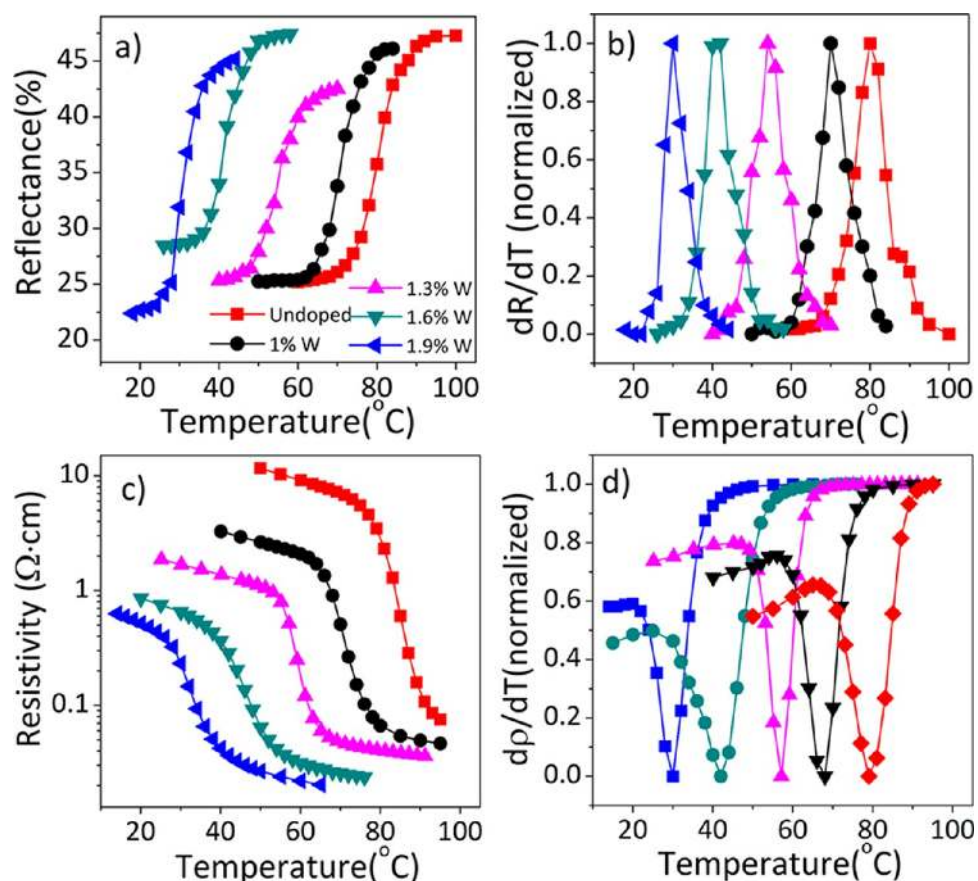


Figure 3. (a) Temperature-dependent reflectivity at 2500 nm from W-doped VO₂ thin films with several different W doping concentrations and (b) first derivatives of optical reflectivity spectra. (c) Temperature-dependent resistivity plots of W-doped VO₂ thin films on fused quartz substrates with several different W doping concentrations and (d) first derivatives of resistivity.

Figure 4a–d displays variable-temperature reflectance measurements of the multilayered structure. At room temperature, all of the layers are insulating. Upon increasing the temperature above T_c for the 1.9% W-doped VO₂, a phase transition occurs in the bottom layer, resulting in the formation of metal–insulator–insulator structure. A shift in the peak and valley positions in the reflectance fringe patterns is observed corresponding to the structural transformation. The reflectance minimum at the valleys of oscillating patterns decreases from 9 to 3% and shifts to longer wavelength (from 2300 to 3000 nm), demonstrating the antireflective property in the near-IR. The optical response of the metal–insulator–insulator structure is maintained until the temperature reaches the phase-change temperature of the 1.3% W-doped VO₂. Around 50 °C, the second metal–insulator transition occurs in the middle layer to form a metal–metal–insulator structure, leading to a shift in the reflectance minimum to shorter wavelengths (from 3000 to 1700 nm). At the reflectance minimum, both reflectance and transmittance exhibit very low values (around 5%), indicating that a strong absorption resonance occurs in the metal–metal insulating phase. This absorption resonance persists at incident angles from 5 to about 50° and reflection increases above 50°

(Supporting Information Figure S11). At temperatures higher than the phase-change temperature of undoped VO₂, all of the layers become metallic VO₂ and the films become reflective throughout the near-IR and IR regions. This suggests that we can engineer the optical responses of multilayered reconfigurable materials, exhibiting abrupt switching from that of a strong light absorber to that of a Drude-like reflector in the near-IR region.

The reflectance at single wavelengths is monitored to better visualize the phase transition of the multilayered films. Figure 4c presents the reflectance collected at 1550 and 3000 nm upon increasing temperature. It is worth noting that the phase-change temperature and steepness of the reflectance change of each layer at T_c are maintained even after integration into the multilayered structure. In addition, the plateaus between the T_c of each layer are also observed, indicating that each transition is discrete, occurring only at the phase-change temperatures of individual layers. Thus, we have demonstrated that VO₂ multilayered thin films, composed of different W doping concentrations, can exhibit multiple phase transition temperatures in a single structure, changing their optical properties at each phase transition.

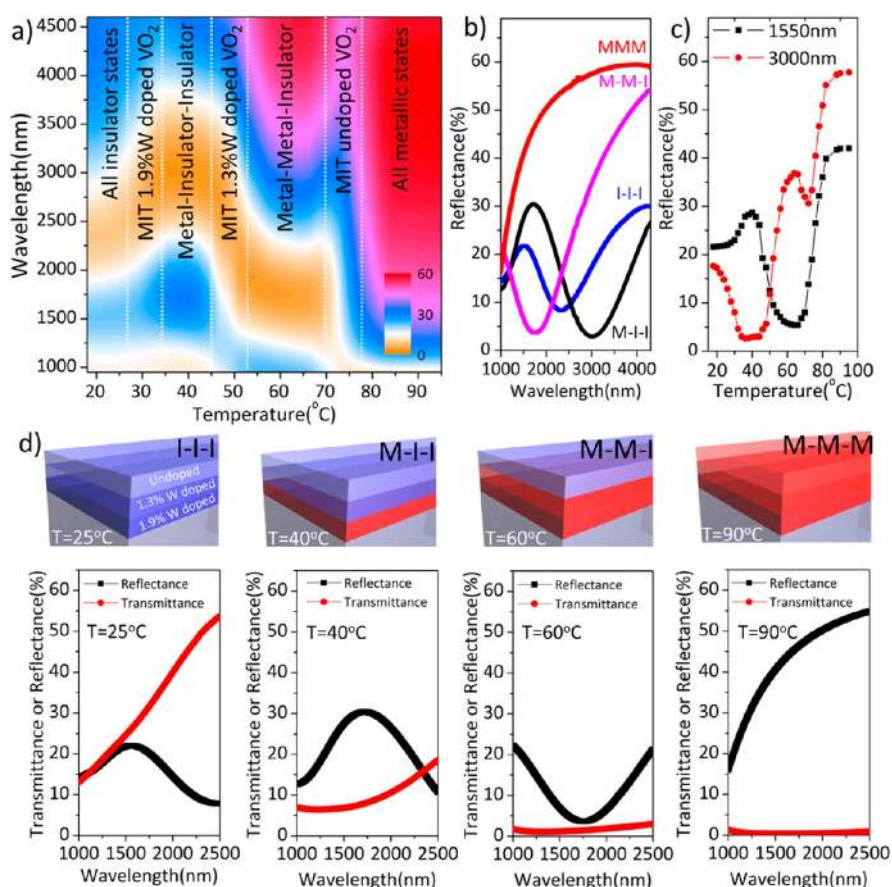


Figure 4. (a) Variable-temperature reflectance spectra of a multilayered VO₂ thin film composed of 1.9% W, 1.3% W, and undoped VO₂ measured at a 20° incident angle and (b) representative reflectance spectra during the phase transition. I and M stand for insulating and metallic phases of VO₂ at each layer. (c) Optical reflectance spectra monitored at 1550 and 3000 nm. (d) Transmittance and reflectance spectra collected at 25, 40, 60, and 90 °C and schematics of the phase of the differentially doped VO₂ layers.

Fabrication of subwavelength plasmonic building blocks from Au colloidal NCs has recently been demonstrated by nanoimprinting to achieve large-area, complex metamaterials.⁷⁷ Coupling this colloidal nanocrystal-based nanoimprinting technique with metallic VO₂ allows for the preparation of switchable plasmonic VO₂ nanostructures. Figure 5a shows the schematic of the process used to form nanostructured VO₂. First, polymer resists are patterned by nanoimprint lithography using a nanostructured Si master designed in size and shape. Then, colloidal NCs are spin-coated on top of the patterned substrate, followed by lift-off of the polymer resist to deposit patterned VO_x thin films. Phase-change VO₂ nanostructures are then obtained after RTA of the patterned VO_x NC films. Figure 5 shows SEM images of planar arrays of VO₂ (b,c) nanopillars and (d,e) nanowires. Nanostructured metallic VO₂ is expected to show a size-dependent dipolar plasmonic resonance as reported in previous studies,^{78–80} although it is a strongly damped resonance due to optical losses.⁶² Figure 5f presents the normalized transmittance spectra of hexagonal arrays of metallic VO₂ nanopillars upon varying the pillar diameter. With increasing diameter from 250 to 460 nm, the resonance peaks are red-shifted from 1520 to 1750 nm.

In order to understand the trend of the transmittance spectra of patterned VO₂, we conducted finite-difference time-domain (FDTD) simulations using the dielectric function of metallic VO₂ derived from spectroscopic ellipsometry. The resonance peaks of simulated spectra are also shifted to longer wavelength from 1600 to 2200 nm with increasing pillar diameter, consistent with the experimental results. The magnitude of the shift in the resonance frequency as a function of pillar size in the measured data is smaller than the values in simulated results. This is not surprising as the morphology of VO₂ nanopillars is known to dramatically affect plasmonic responses⁶² and that is not captured in the simulations. The VO₂ nanostructures formed by the RTA of 4 nm diameter nanocrystals limit grain growth to about 40 nm, and thus the granular features of the plasmonic VO₂ nanostructures could be responsible for the discrepancy between experiment and simulation.

Coupling lateral patterning of subwavelength VO₂ nanostructures by nanoimprint lithography with the vertical structuring of multilayered thin films, we form three-dimensional VO₂ nanopillar arrays where each pillar consists of a vertical stack of doped VO₂ with different W doping concentrations. Figure 5d displays

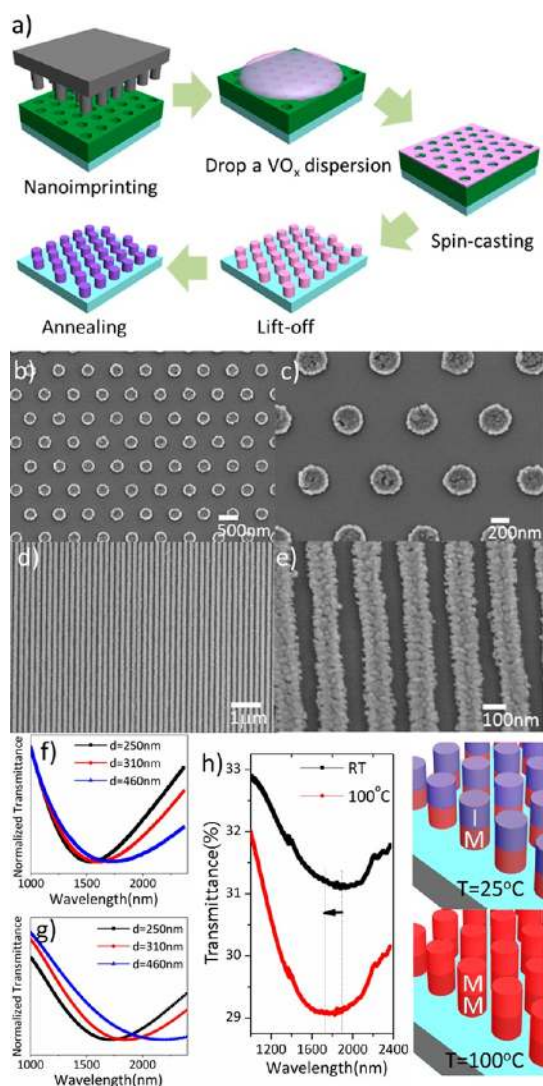


Figure 5. (a) Schematic of subwavelength VO_2 nanostructure fabrication using nanoimprint lithography. SEM images of VO_2 nanostructure arrays of (b,c) hexagonal lattice of nanopillars and (d,e) nanowires. (f) Experimental and (g) simulated transmittance of VO_2 nanopillar arrays of varying diameters. (h) Transmittance of layered VO_2 nanopillar arrays vertically stacked with 3% W and undoped VO_2 . Transmittance spectra are collected at 25 and 100 °C.

a schematic of nanopillar arrays composed of 3% W-doped and undoped VO_2 . A three-dimensional,

hierarchical nanostructure is fabricated by sequential spin-coating of 3% W-doped VO_x and undoped VO_x onto the polymer resist. In order to prevent intermixing of NCs between two layers, mild heating at typically 100 °C for 30 min is applied after the first layer is deposited. As above, polymer resists are lifted off using acetone and films are thermally annealed to obtain patterned VO_2 . At room temperature, 3% W-doped VO_2 is metallic, forming metal–insulator structures in each pillar. The dipolar plasmonic response of the nanopillar arrays is observed by the broad peak located at about 1900 nm. Upon increasing the temperature above the T_c of undoped VO_2 , the upper layer in the pillar changes to metallic and the resonance of the nanostructures blue shifts from approximately 1900 to 1750 nm. This trend is consistent with FDTD simulations (Supporting Information Figure S12). The shift of the resonance peaks to shorter wavelengths is consistent with the second phase transition at the upper layer effectively causing an increase in the height of the metallic nanopillars, resulting in a shift of the resonance peaks to shorter wavelengths.^{81,82}

CONCLUSION

In summary, we demonstrate solution-processed tunable VO_2 metamaterials using colloidal VO_x NCs. Colloidal VO_x NCs are synthesized using vanadium oxychloride precursors in the presence of 1-octadecanol and oleylamine solvent mixture. Thermo-chromic VO_2 are obtained by rapid thermal annealing of VO_x NCs. Stable dispersions of the colloidal NCs are readily processed by conventional deposition techniques and nanostructured using nanoimprinting. Tungsten doping is readily controlled by changing the precursor concentration during the synthesis, allowing for a systematic change of the phase transition behaviors. Solution-based fabrication and controlled doping allow for integration of doped VO_2 building blocks into complex architectures including switchable metal–dielectric multilayered structures composed of W-doped VO_2 with different dopant concentrations and patterned layered structures. The versatility and processability of solution-based fabrication provides a route to integrate switchable VO_2 building blocks into a variety of nanostructured metamaterials to modulate the optical response in real-time.

EXPERIMENTAL SECTION

Materials. All chemicals are used as purchased without any further purification. Vanadium(V) oxychloride (99%) and oleylamine (technical grade, 70%) are purchased from Sigma Aldrich. 1-Octadecanol (97%) is purchased from Alfa Aesar. Tungsten(VI) chloride (99.9+%) is purchased from Acros Organics.

Synthesis of VO_x Nanocrystals. 1-Octadecanol (7.92 g) and oleylamine (30 mL) are added to a 125 mL three-neck flask and degassed at 125 °C for 1 h. Then, 0.4 mL of vanadium oxychloride is added into the reaction mixtures and heated to 250 °C at a rate of 10 °C/min in ambient air environment. The temperature

is maintained for 20 min, allowing for the nanocrystal growth. Purification is conducted by adding toluene and excess methanol followed by centrifugation at 6000 rpm for 2 min. Precipitated nanocrystals are redispersed in anhydrous hexane and stored under N_2 environment to prevent oxidation of nanocrystals.

Rapid Thermal Annealing for Structure Transformation from VO_x to Monoclinic VO_2 . Colloidal VO_x nanocrystals are deposited on the substrates by spin-coating, typically at 1500 rpm for 30 s. Nanocrystal thin films are annealed using rapid thermal annealing (ULVAC MILA-3000) by ramping to 500 °C in 10 s and annealing for 5 min under 1 mTorr of air environment.

Nanoimprint Lithography. Vanadium oxide (VO₂)-based plasmonic nanostructures are fabricated by nanoimprint lithography and lift-off using VO_x colloidal nanocrystals. Commercial float glass (Delta-Technologies) is cleaned by ultrasonication with acetone and isopropyl alcohol for 10 min and rinsed with deionized water. Nanoimprinting lithography is done using a Nanonex (NX-2600) nanoimprinting system. A thermal nanoimprint resist (NXR-1000) film is made by spin-coating at 3000 rpm for 1 min and baked at 150 °C for 5 min. A nanostructured Si-based template is used as a master stamp. The thermal resist coated glass substrate is covered by a master stamp, and then the stack of the stamp and substrate is heated and pressed up to 130 °C and 300 psi for 5 min in order to fill the cavity of the stack, and then it is cooled for demolding. After imprinting, an oxygen “descum” process is performed on the samples in a Technics dry etching tool for 35 s with 80 sccm O₂ and 150 W power, in order to remove residual polymer layers. To fabricate VO₂-based plasmonic nanostructures, VO_x nanocrystals are spin-coated on the imprinted pattern on the glass substrate. Then, the polymer resist is removed by lift-off in acetone for 30 s to obtain the inverted VO_x patterns. Nanostructured thermochromic VO₂ is obtained after rapid thermal annealing at 500 °C for 5 min under 1 mTorr air.

Structural Characterization. TEM images and electron diffraction patterns are collected using a JEM-1400 microscope equipped with a SC1000 ORIUS CCD camera operating at 120 kV. Scanning electron microscopy (SEM) and energy-dispersive X-ray spectroscopy was performed on a JEOL 7500F HRSEM. Powder X-ray diffraction, in-plane X-ray diffraction, and small-angle X-ray scattering are collected using a Rigaku Smartlab high-resolution diffractometer with Cu K α radiation ($\lambda = 1.5416 \text{ \AA}$). The scattering curve is fit using Rigaku NANO-Solver software (shown in red line) with a spherical model and particle size distribution corresponding to the Schultz distribution function. Atomic force microscopy images are obtained using a MFP-3D AFM (Asylum Research). Temperature-dependent resistivity measurements are performed using a variable-temperature microprobe system K20 from MMR technologies coupled with a HP 4145B semiconductor parameter analyzer.

Optical Characterization. Variable-temperature specular reflectance spectra are collected using a Fourier transform infrared (FTIR) spectrometer with a Seagull variable-angle reflection accessory (Harrick Scientific) equipped with the aluminum heating stage. Ellipsometry spectra of VO₂ on quartz are collected using a M-2000 ellipsometer (J.A. Woollam Co.). For the ellipsometric measurement, the complex reflectance ratio is measured from 370 to 1680 nm at 45, 55, 65, and 75°. Dielectric functions of VO₂ thin films deposited on SiO₂/Si wafers are extracted by fitting with Drude–Lorentz oscillators using the CompleteEASE software package (J.A. Woollam Co.). Full-wave electromagnetic field calculations are performed using the commercially available simulation software package FDTD Solutions from Lumerical, Inc. A unit cell of the investigated structure is simulated using periodic boundary conditions along the *x* and *y* axes and perfectly matched layers along the direction of propagation of the electromagnetic waves (*z* axis). Plane waves are launched incident to the unit cell along the +*z* direction, and transmittance is monitored with a power monitor placed behind the structure. Electric and magnetic fields are detected within the frequency profile monitors. To model VO₂ nanocrystals in the simulations, we use measured dispersion data.

Conflict of Interest: The authors declare no competing financial interest.

Acknowledgment. T.J.P., S.-H.H., H.C., N.E., C.R.K., and C.B.M. were supported by the Office of Naval Research Multidisciplinary University Research Initiative Award No. ONR-N00014-10-1-0942, providing primary support for the synthesis of VO_x nanocrystals; structural characterization of VO_x nanocrystals and VO₂ thin films by TEM, PXRD, SAXS, and AFM; optical characterization; nanoimprinting of VO₂ nanostructures; FDTD simulations; and research oversight. E.A.G.'s temperature-dependent electrical measurement of VO₂ thin films was supported by the U.S. Department of Energy Office of Basic Energy Sciences, Division of Materials Science and Engineering Award No. DE-SC0002158. T.R.G.'s

contribution to the structural analysis on the oxide NCs in this study was partially supported by the Nano/Bio Interface Center through the National Science Foundation NSEC DMR08-32802. C.B.M. is grateful for the support of Richard Perry University Professorship.

Supporting Information Available: Details regarding the nanocrystal synthesis, additional TEM and HRTEM images, small-angle X-ray scattering and wide-angle X-ray diffraction results, temperature-dependent resistivity data, AFM images, transmittance and reflectance spectra, and a simulation result. This material is available free of charge via the Internet at <http://pubs.acs.org>.

REFERENCES AND NOTES

- Soukoulis, C. M.; Wegener, M. Past Achievements and Future Challenges in the Development of Three-Dimensional Photonic Metamaterials. *Nat. Photonics* **2011**, *5*, 523–530.
- Zheludev, N. I.; Kivshar, Y. S. From Metamaterials to Metadevices. *Nat. Mater.* **2012**, *11*, 917–924.
- Boltasseva, A.; Atwater, H. A. Low-Loss Plasmonic Metamaterials. *Science* **2011**, *331*, 290–291.
- Shelby, R. A.; Smith, D. R.; Schultz, S. Experimental Verification of a Negative Index of Refraction. *Science* **2001**, *292*, 77–79.
- Valentine, J.; Zhang, S.; Zentgraf, T.; Ulin-Avila, E.; Genov, D. A.; Bartal, G.; Zhang, X. Three-Dimensional Optical Metamaterial with a Negative Refractive Index. *Nature* **2008**, *455*, 376–379.
- Smith, D. R.; Pendry, J. B.; Wiltshire, M. C. K. Metamaterials and Negative Refractive Index. *Science* **2004**, *305*, 788–792.
- Pendry, J. B. Negative Refraction Makes a Perfect Lens. *Phys. Rev. Lett.* **2000**, *85*, 3966–3969.
- Fang, N.; Lee, H.; Sun, C.; Zhang, X. Sub-Diffraction-Limited Optical Imaging with a Silver Superlens. *Science* **2005**, *308*, 534–537.
- Schurig, D.; Mock, J. J.; Justice, B. J.; Cummer, S. A.; Pendry, J. B.; Starr, A. F.; Smith, D. R. Metamaterial Electromagnetic Cloak at Microwave Frequencies. *Science* **2006**, *314*, 977–980.
- Alù, A.; Engheta, N. Achieving Transparency with Plasmonic and Metamaterial Coatings. *Phys. Rev. E* **2005**, *72*, 016623.
- Liu, N.; Mesch, M.; Weiss, T.; Hentschel, M.; Giessen, H. Infrared Perfect Absorber and Its Application as Plasmonic Sensor. *Nano Lett.* **2010**, *10*, 2342–2348.
- Anker, J. N.; Hall, W. P.; Lyandres, O.; Shah, N. C.; Zhao, J.; Duyn, R. P. V. Biosensing with Plasmonic Nanosensors. *Nat. Mater.* **2008**, *7*, 442–453.
- Pryce, I. M.; Aydin, K.; Kelaita, Y. A.; Briggs, R. M.; Atwater, H. A. Highly Strained Compliant Optical Metamaterials with Large Frequency Tunability. *Nano Lett.* **2010**, *10*, 4222–4227.
- Hess, O.; Pendry, J. B.; Maier, S. A.; Oulton, R. F.; Hamm, J. M.; Tsakmakidis, K. L. Active Nanoplasmonic Metamaterials. *Nat. Mater.* **2012**, *11*, 573–584.
- Boardman, A. D.; Grimalsky, V. V.; Kivshar, Y. S.; Koshevaya, S. V.; Lapine, M.; Litchinitser, N. M.; Malnev, V. N.; Noginov, M.; Rapoport, Y. G.; Shalae, V. M. Active and Tunable Metamaterials. *Laser Photonics Rev.* **2010**, *5*, 287–307.
- Ou, J. Y.; Plum, E.; Jiang, L.; Zheludev, N. I. Reconfigurable Photonic Metamaterials. *Nano Lett.* **2011**, *11*, 2142–2144.
- Hsiao, V. K. S.; Zheng, Y. B.; Juluri, B. K.; Huang, T. J. Light-Driven Plasmonic Switches Based on Au Nanodisk Arrays and Photoresponsive Liquid Crystals. *Adv. Mater.* **2008**, *20*, 3528–3532.
- Krasavin, A. V.; Zheludev, N. I. Active Plasmonics: Controlling Signals in Au/Ga Waveguide Using Nanoscale Structural Transformations. *Appl. Phys. Lett.* **2004**, *84*, 1416–1418.
- Wang, Z.; Chumanov, G. WO₃ Sol–Gel Modified Ag Nanoparticle Arrays for Electrochemical Modulation of Surface Plasmon Resonance. *Adv. Mater.* **2003**, *15*, 1285–1289.
- Pernice, W. H. P.; Bhaskaran, H. Photonic Non-volatile Memories Using Phase Change Materials. *Appl. Phys. Lett.* **2012**, *101*, 171101.

21. Sámson, Z. L.; MacDonald, K. F.; Angelis, F. D.; Gholipour, B.; Knight, K.; Huang, C. C.; Fabrizio, E. D.; Hewak, D. W.; Zheludev, N. I. Metamaterial Electro-optic Switch of Nano-scale Thickness. *Appl. Phys. Lett.* **2010**, *96*, 143105.
22. Maaza, M.; Nemraoui, O.; Sella, C.; Beye, A. C.; Baruch-Barak, B. Thermal Induced Tunability of Surface Plasmon Resonance in Au-VO₂ Nano-Photonics. *Opt. Commun.* **2005**, *254*, 188–195.
23. Goodenough, J. B. Anomalous Properties of the Vanadium Oxides. *Annu. Rev. Mater. Sci.* **1971**, *1*, 101–138.
24. Morin, F. J. Oxides Which Show a Metal-to-Insulator Transition at the Neel Temperature. *Phys. Rev. Lett.* **1959**, *3*, 34–36.
25. Tselev, A.; Luk'yanchuk, I. A.; Ivanov, I. N.; Budai, J. D.; Tischler, J. Z.; Strelcov, E.; Kolmakov, A.; Kalinin, S. V. Symmetry Relationship and Strain-Induced Transitions between Insulating M1 and M2 and Metallic R Phases of Vanadium Dioxide. *Nano Lett.* **2010**, *10*, 4409–4416.
26. Cao, J.; Ertekin, E.; Srinivasan, V.; Fan, W.; Huang, S.; Zheng, H.; Yim, J. W. L.; Khanal, D. R.; Ogletree, D. F.; Grossman, J. C.; *et al.* Strain Engineering and One-Dimensional Organization of Metal-Insulator Domains in Single-Crystal Vanadium Dioxide Beams. *Nat. Nanotechnol.* **2009**, *4*, 732–737.
27. Ruzmetov, D.; Gopalakrishnan, G.; Ko, C.; Narayanamurti, V.; Ramanathan, S. Three-Terminal Field Effect Devices Utilizing Thin Film Vanadium Oxide as the Channel Layer. *J. Appl. Phys.* **2010**, *107*, 114516.
28. Nakano, M.; Shibuya, K.; Okuyama, D.; Hatano, T.; Ono, S.; Kawasaki, M.; Iwasa, Y.; Tokura, Y. Collective Bulk Carrier Delocalization Driven by Electrostatic Surface Charge Accumulation. *Nature* **2012**, *487*, 459–462.
29. Jeong, J.; Aetukuri, N.; Graf, T.; Schladt, T. D.; Samant, M. G.; Parkin, S. S. P. Suppression of Metal-Insulator Transition in VO₂ by Electric Field-Induced Oxygen Vacancy Formation. *Science* **2013**, *339*, 1402–1405.
30. Granqvist, C. G. Solar Energy Materials. *Adv. Mater.* **2003**, *15*, 1789–1803.
31. Granqvist, C. G. Transparent Conductors as Solar Energy Materials: A Panoramic Review. *Sol. Energy Mater. Sol. Cells* **2007**, *91*, 1529–1598.
32. Gea, L. A.; Boatner, L. A. Optical Switching of Coherent VO₂ Precipitates Formed in Sapphire by Ion Implantation and Annealing. *Appl. Phys. Lett.* **1996**, *68*, 3081–3083.
33. Driscoll, T.; Kim, H.-T.; Chae, B.-G.; Kim, B.-J.; Lee, Y.-W.; Jokerst, N. M.; Palit, S.; Smith, D. R.; Ventra, M. D.; Basov, D. N. Memory Metamaterials. *Science* **2009**, *325*, 1518–1521.
34. Lee, M.-J.; Park, Y.; Suh, D.-S.; Lee, E.-H.; Seo, S.; Kim, D.-C.; Jung, R.; Kang, B.-S.; Ahn, S.-E.; Lee, C. B.; *et al.* Two Series Oxide Resistors Applicable to High Speed and High Density Nonvolatile Memory. *Adv. Mater.* **2007**, *19*, 3919–3923.
35. Coy, H.; Cabrera, R.; Sepúlveda, N.; Fernández, F. E. Optoelectronic and All-Optical Multiple Memory States in Vanadium Dioxide. *J. Appl. Phys.* **2010**, *108*, 113115.
36. Stefanovich, G.; Pergament, A.; Stefanovich, D. Electrical Switching and Mott Transition in VO₂. *J. Phys.: Condens. Matter* **2000**, *12*, 8837–8845.
37. Yang, Z.; Ko, C.; Ramanathan, S. Oxide Electronics Utilizing Ultrafast Metal-Insulator Transitions. *Annu. Rev. Mater. Res.* **2011**, *41*, 337–367.
38. Liu, M.; Hwang, H. Y.; Tao, H.; Strikwerda, A. C.; Fan, K.; Keiser, G. R.; Sternbach, A. J.; West, K. G.; Kittiwatanakul, S.; Lu, J.; *et al.* Terahertz-Field-Induced Insulator-to-Metal Transition in Vanadium Dioxide Metamaterial. *Nature* **2012**, *487*, 345–348.
39. Driscoll, T.; Palit, S.; Qazilbash, M. M.; Brehm, M.; Keilmann, F.; Chae, B.-G.; Yun, S.-J.; Kim, H.-T.; Cho, S. Y.; Jokerst, N. M.; *et al.* Dynamic Tuning of an Infrared Hybrid-Metamaterial Resonance Using Vanadium Dioxide. *Appl. Phys. Lett.* **2008**, *93*, 024101.
40. Kruger, B. A.; Joushaghani, A.; Poon, J. K. S. Design of Electrically Driven Hybrid Vanadium Dioxide (VO₂) Plasmonic Switches. *Opt. Express* **2012**, *20*, 23598–23609.
41. Kats, M. A.; Blanchard, R.; Genevet, P.; Yang, Z.; Qazilbash, M. M.; Basov, D. N.; Ramanathan, S.; Capasso, F. Thermal Tuning of Mid-infrared Plasmonic Antenna Arrays Using a Phase Change Material. *Opt. Lett.* **2012**, *38*, 368–370.
42. Dicken, M. J.; Aydin, K.; Pryce, I. M.; Sweatlock, L. A.; Boyd, E. M.; Walavalkar, S.; Ma, J.; Atwater, H. A. Frequency Tunable Near-Infrared Metamaterials Based on VO₂ Phase Transition. *Opt. Express* **2009**, *17*, 18330–18339.
43. Sweatlock, L. A.; Diest, K. Vanadium Dioxide Based Plasmonic Modulators. *Opt. Express* **2012**, *20*, 8700–8709.
44. Béteille, F.; Morineau, R.; Nagano, J. L. M. Switching Properties of V_{1-x}Ti_xO₂ Thin Films Deposited from Alkoxides. *Mater. Res. Bull.* **1997**, *32*, 1109–1117.
45. Partlow, D. P.; Gurkovich, S. R.; Radford, K. C.; Denes, L. J. Switchable Vanadium Oxide Films by a Sol–Gel Process. *J. Appl. Phys.* **1991**, *70*, 443–452.
46. Lopez, R.; Boatner, L. A.; Haynes, T. E.; Feldman, L. C.; Haglund, R. F., Jr. Synthesis and Characterization of Size-Controlled Vanadium Dioxide Nanocrystals in a Fused Silica Matrix. *J. Appl. Phys.* **2002**, *92*, 4031–4036.
47. Ruzmetov, D.; Zawilski, K.; Narayanamurti, V.; Ramanathan, S. Structure-Functional Property Relationships in RF-Sputtered Vanadium Oxide Thin Films. *J. Appl. Phys.* **2007**, *102*, 113715.
48. Guiton, B. S.; Gu, Q.; Prieto, A. L.; Gudixsen, M. S.; Park, H. Single-Crystalline Vanadium Dioxide Nanowires with Rectangular Cross Sections. *J. Am. Chem. Soc.* **2005**, *127*, 498–499.
49. Kim, D. H.; Kwok, H. S. Pulsed Laser Deposition of VO₂ Thin Films. *Appl. Phys. Lett.* **1994**, *65*, 3188–3190.
50. Jorgenson, G. V.; Lee, J. C. Doped Vanadium Oxide for Optical Switching Films. *Sol. Energy Mater.* **1986**, *14*, 205–214.
51. Sargent, E. H. Infrared Photovoltaics Made by Solution Processing. *Nat. Photonics* **2009**, *3*, 325–331.
52. Gur, I.; Fromer, N. A.; Geier, M. L.; Alivisatos, A. P. Air-Stable All-Inorganic Nanocrystal Solar Cells Processed from Solution. *Science* **2005**, *310*, 462–465.
53. Böberl, M.; Kovalenko, M. V.; Gamerith, S.; List, E. J. W.; Heiss, W. Inkjet-Printed Nanocrystal Photodetectors Operating up to 3 μm Wavelengths. *Adv. Mater.* **2007**, *19*, 3574–3578.
54. Lewis, J. A. Direct-Write Assembly of Ceramics from Colloidal Inks. *Curr. Opin. Solid State Mater. Sci.* **2002**, *6*, 245–250.
55. Niederberger, M. Nonaqueous Sol–Gel Routes to Metal Oxide Nanoparticles. *Acc. Chem. Res.* **2007**, *40*, 793–800.
56. Katzke, H.; Tolédano, P.; Depmeier, W. Theory of Morphotropic Transformations in Vanadium Oxides. *Phys. Rev. B* **2004**, *68*, 024109.
57. Griffiths, C. H.; Eastwood, H. K. Influence of Stoichiometry on the Metal-Semiconductor Transition in Vanadium Dioxide. *J. Appl. Phys.* **1974**, *45*, 2201–2206.
58. Okimura, K.; Sakai, J.; Ramanathan, S. *In Situ* X-ray Diffraction Studies on Epitaxial VO₂ Films Grown on c-Al₂O₃ during Thermally Induced Insulator Metal Transition. *J. Appl. Phys.* **2010**, *107*, 063503.
59. Fu, D.; Liu, K.; Tao, T.; Lo, K.; Cheng, C.; Liu, B.; Zhang, R.; Bechtel, H. A.; Wu, J. Comprehensive Study of the Metal-Insulator Transition in Pulsed Laser Deposited Epitaxial VO₂ Thin Films. *J. Appl. Phys.* **2013**, *113*, 043707.
60. Cui, Y.; Ramanathan, S. Substrate Effects on Metal-Insulator Transition Characteristics of rf-Sputtered Epitaxial VO₂ Thin Films. *J. Vac. Sci. Technol., A* **2011**, *29*, 041502.
61. Lopez, R.; Haynes, T. E.; Boatner, L. A.; Feldman, L. C.; Haglund, R. F., Jr. Size Effects in the Structural Phase Transition of VO₂ Nanoparticles. *Phys. Rev. B* **2002**, *65*, 224113.
62. Appavoo, K.; Lei, D. Y.; Sonnefraud, Y.; Wang, B.; Pantelides, S. T.; Maier, S. A.; Haglund, R. F., Jr. Role of Defects in the Phase Transition of VO₂ Nanoparticles Probed by Plasmon Resonance Spectroscopy. *Nano Lett.* **2012**, *12*, 780–786.
63. Brassard, D.; Fourmaux, S.; Jean-Jacques, M.; Kieffer, J. C.; Khakania, M. A. E. Grain Size Effect on the Semiconductor-Metal Phase Transition Characteristics of Magnetron-Sputtered VO₂ Thin Films. *Appl. Phys. Lett.* **2005**, *87*, 051910.
64. Strelcov, E.; Tselev, A.; Ivanov, I.; Budai, J. D.; Zhang, J.; Tischler, J. Z.; Kravchenko, I.; Kalinin, S. V.; Kolmakov, A.

- Doping-Based Stabilization of the M2 Phase in Free-Standing VO₂ Nanostructures at Room Temperature. *Nano Lett.* **2012**, *12*, 6198–6205.
65. Wei, J.; Ji, H.; Guo, W.; Nevidomskyy, A. H.; Natelson, D. Hydrogen Stabilization of Metallic Vanadium Dioxide in Single-Crystal Nanobeams. *Nat. Nanotechnol.* **2012**, *7*, 357–362.
66. Mocatta, D.; Cohen, G.; Schattner, J.; Millo, O.; Rabani, E.; Banin, U. Heavily Doped Semiconductor Nanocrystal Quantum Dots. *Science* **2011**, *332*, 77–81.
67. Ba, J.; Rohlfing, D. F.; Feldhoff, A.; Brezesinski, T.; Djerdj, I.; Wark, M.; Niederberger, M. Nonaqueous Synthesis of Uniform Indium Tin Oxide Nanocrystals and Their Electrical Conductivity in Dependence of the Tin Oxide Concentration. *Chem. Mater.* **2006**, *18*, 2848–2854.
68. Mikulec, F. V.; Kuno, M.; Bennati, M.; Hall, D. A.; Griffin, R. G.; Bawendi, M. G. Organometallic Synthesis and Spectroscopic Characterization of Manganese-Doped CdSe Nanocrystals. *J. Am. Chem. Soc.* **2000**, *122*, 2532–2540.
69. Buonsanti, R.; Llordes, A.; Aloni, S.; Helms, B. A.; Milliron, D. J. Tunable Infrared Absorption and Visible Transparency of Colloidal Aluminum-Doped Zinc Oxide Nanocrystals. *Nano Lett.* **2011**, *11*, 4706–4710.
70. Gordon, T. R.; Paik, T.; Klein, D. R.; Naik, G. V.; Caglayan, H.; Boltasseva, A.; Murray, C. B. Shape-Dependent Plasmonic Response and Directed Self-Assembly in a New Semiconductor Building Block, Indium-Doped Cadmium Oxide (ICO). *Nano Lett.* **2013**, *13*, 2857–2863.
71. Norris, D. J.; Yao, N.; Charnock, F. T.; Kennedy, T. A. High-Quality Manganese-Doped ZnSe Nanocrystals. *Nano Lett.* **2001**, *1*, 3–7.
72. Schwartz, D. A.; Norberg, N. S.; Nguyen, Q. P.; Parker, J. M.; Gamelin, D. R. Magnetic Quantum Dots: Synthesis, Spectroscopy, and Magnetism of Co²⁺- and Ni²⁺-Doped ZnO Nanocrystals. *J. Am. Chem. Soc.* **2003**, *125*, 13205–13218.
73. Nag, J.; Haglund, R. F., Jr. Synthesis of Vanadium Dioxide Thin Films and Nanoparticles. *J. Phys.: Condens. Matter* **2008**, *20*, 264016.
74. Bouhafs, D.; Moussi, A.; Chikouche, A.; Ruiz, J. M. Design and Simulation of Antireflection Coating Systems for Optoelectronic Devices: Application to Silicon Solar Cells. *Sol. Energy Mater. Sol. Cells* **1998**, *52*, 79–93.
75. Dionne, J. A.; Sweatlock, L. A.; Atwater, H. A.; Polman, A. Planar Metal Plasmon Waveguides: Frequency-Dependent Dispersion, Propagation, Localization, and Loss beyond the Free Electron Model. *Phys. Rev. B* **2005**, *72*, 075405.
76. Kats, M. A.; Sharma, D.; Lin, J.; Genevet, P.; Blanchard, R.; Yang, Z.; Qazilbash, M. M.; Basov, D. N.; Ramanathan, S.; Capasso, F. Ultra-thin Perfect Absorber Employing a Tunable Phase Change Material. *Appl. Phys. Lett.* **2012**, *101*, 221101.
77. Fafarman, A. T.; Hong, S.-H.; Caglayan, H.; Ye, X.; Diroll, B. T.; Paik, T.; Engheta, N.; Murray, C. B.; Kagan, C. R. Chemically Tailored Dielectric-to-Metal Transition for the Design of Metamaterials from Nanoimprinted Colloidal Nanocrystals. *Nano Lett.* **2013**, *13*, 350–357.
78. Bai, H.; Cortie, M. B.; Maarroof, A. I.; Dowd, A.; Kealley, C.; Smith, G. B. The Preparation of a Plasmonically Resonant VO₂ Thermochromic Pigment. *Nanotechnology* **2009**, *20*, 085607.
79. Lopez, R.; Haynes, T. E.; Boatner, L. A.; Feldman, L. C.; Haglund, R. F., Jr. Temperature-Controlled Surface Plasmon Resonance in VO₂ Nanorods. *Opt. Lett.* **2002**, *27*, 1327–1329.
80. Lopez, R.; Feldman, L. C.; Haglund, R. F., Jr. Size-Dependent Optical Properties of VO₂ Nanoparticle Arrays. *Phys. Rev. Lett.* **2004**, *93*, 177403.
81. Zheng, Y. B.; Juluri, B. K.; Mao, X.; Walker, T. R.; Huang, T. J. Systematic Investigation of Localized Surface Plasmon Resonance of Long-Range Ordered Au Nanodisk Arrays. *J. Appl. Phys.* **2008**, *103*, 014308.
82. Barchiesi, D.; Kessentini, S.; Guillot, N.; de la Chapelle, M. L.; Grosjes, T. Localized Surface Plasmon Resonance in Arrays of Nano-Gold Cylinders: Inverse Problem and Propagation of Uncertainties. *Opt. Express* **2013**, *21*, 2245–2262.